Directional short wind wave spectra derived from the sea surface photography

M. V. Yurovskaya,[1,2] V. A. Dulov,[1,2] B. Chapron,[3,4] and V. N. Kudryavtsev[1,4]

[1] New field measurements of 2-D wave number short wind wave spectra in the wavelength range from few millimeters to few decimeters are reported and discussed. The measurement method is based on stereophotography and image brightness contrast processing. As found, the spectra of decimeter waves are almost isotropic and weakly dependent on the wind speed. Both directional anisotropy and wind sensitivity rapidly increase at wave numbers larger than 100 rad/m. These aspects are consistent with other previously reported optical and radar data. Following these new in situ measurements, a revision of a semiempirical model of short wind wave spectrum is suggested. This revised model can readily be implemented in other studies (radar scattering, air-sea interaction issues) where detailed knowledge of short wind wave spectra is crucial.

Citation: Yurovskaya, M. V., V. A. Dulov, B. Chapron, and V. N. Kudryavtsev (2013), Directional short wind wave spectra derived from the sea surface photography, *J. Geophys. Res. Oceans*, *118*, 4380–4394, doi:10.1002/jgrc.20296.

1. Introduction

[2] Predictions of the momentum, heat and gas transfer at the sea surface are still poor, partly because of the lack of reliable field observations of small-scale surface waves. An improved statistical description of the short wave spectrum is a key to provide more accurate estimates of the exchange processes between the ocean and atmosphere. From an experimental point of view, wave number spectral measurements have become feasible in wind wave facilities, but are still very difficult to obtain in the field. From laboratory experiments [e.g., *Jähne and Riemer*, 1990; *Hwang*, 1993; *Zhang*, 1995], a strong high-frequency cutoff, independent of wind conditions, and a peak of the saturation spectrum in the vicinity of 800 rad/m have been revealed. The latter has then been associated to the generation of parasitic capillaries [e.g., *Kudryavtsev et al.*, 1999]. From field experiments, *Banner et al.* [1989] reported stereographic measurements taken from an oil platform, but limited to pure gravity waves (from 20 cm to 1.6 m). For this spectral range, a very weak wind dependency was reported. Very few field measurements of wave number spectra of short ocean waves in the gravity-capillary and capillary range are available [*Hara et al.*, 1994; *Hwang et al.*, 1996; *Hara et al.*, 1998]. These investigations led to spectral shapes and wind dependency that significantly differ from those observed in laboratory conditions.

[3] From a remote sensing perspective, small-scale wave spectra are also essential. Sun reflected measurements first yield very robust information about the statistics of surface slopes [*Cox and Munk*, 1954], later confirmed using satellite observations [*Breon and Henriot*, 2006]. Radar data purposefully excluded from their empirical development, *Elfouhaily et al.* [1997] tailored the spectral energy in the short-scale gravity and capillary bands to be consistent with the Cox and Munk dependence of mean-square slope on wind speed. Including radar data, numerous attempts [e.g., *Fung and Lee*, 1982; *Donelan and Pierson*, 1987; *Romeiser et al.*, 1997] strongly built on active microwave observations to more precisely invert short-wave spectral properties. To note, laboratory radar backscatter observations were the base measurements to derive the often-used wind wave growth parameter [*Plant*, 1986]. Dual-frequency radar backscatter measurements from a tower [*Lawner and Moore*, 1984] were analyzed to infer capillary and short-scale gravity wave spectra using the small perturbation scattering model to interpret the data. More recently, *Hwang* [2011] also used different radar frequencies from 1.4 to 19.3 GHz for analysis of the short-scale spectral slopes and wind exponent. From passive microwave sensors, *Trokhimovski* [2000] and *Trokhimovski and Irisov* [2001] proposed to use polarimetric measurements collected at several viewing angles and frequencies to convert the observed brightness temperatures to the mean-square slope of tilting waves and curvature spectral density in the gravity-capillary interval. Finally, the level of acoustic noise is also currently explored as a potential source of information related to the still poorly known directional

[1]Remote Sensing Department, Marine Hydrophysical Institute, Sevastopol, Ukraine.
[2]Advisory and research company, DVS Ltd., Sevastopol, Ukraine.
[3]Ifremer, Laboratoire Océanographie Spatiale, Plouzané, France.
[4]Russian State Hydrometeorological University, Satellite Oceanography Laboratory (SOLab), Saint Petersburg, Russia.

Corresponding author: M. V. Yurovskaya, Remote Sensing Department, Marine Hydrophysical Institute, 2 Kapitanskaya St., Sevastopol 99011, Ukraine. (mvkosnik@gmail.com)

spectrum of short gravity-capillary waves [*Farrell and Munk*, 2008].

[4] All these indirect estimations can certainly be assembled to provide a consistent approach. Yet, as often recognized, possible limitation of the scattering theory [e.g., *Guérin et al.*, 2010; *Mouche et al.*, 2007], as well as exact knowledge of the effects of higher order statistics [*Chapron et al.*, 2000; *Bringer et al.*, 2012, 2013], singular geometrical [*Voronovich and Zavorotny*, 2001; *Kudryavtsev et al.*, 2005], and/or foam impacts [*Reul and Chapron*, 2003], all somehow preclude a simple short-scale spectral inversion. To minimize such difficulties, a suggested possibility is to solely analyze the polarization contributions from radar backscatter signals [e.g., *Chapron et al.*, 1997; *Kudryavtsev et al.*, 2013].

[5] The main goal of this paper is thus first to report new field stereophotograph measurements of 2-D wave number spectra of short wind waves in the wavelength range from few millimeters to few decimeters. Then, on the basis of these new measurements, we propose to revise the semiempirical model of short wind wave spectra previously developed [*Kudryavtsev et al.*, 1999, 2003, 2005; *Kudryavtsev and Johannessen*, 2004]. In these models, solutions were derived considering the energy balance equation under the joint action of the wind forcing, viscous dissipation, nonlinear dissipation term related to wave breaking and microbreaking, and generation of parasitic capillaries. Accordingly, the new in situ observations provide additional constraints to help refine a two-dimensional wave number spectrum valid over the short-scale gravity and capillary large wave numbers, analytically amenable to different usage.

[6] The paper is organized as follows. In section 2, we describe the field experiment. A brief summary of the method to retrieve short wind wave spectra [*Kosnik and Dulov*, 2011] is outlined in section 3. Results and comparisons with previous observations including optical and multifrequency radar measurements are presented in section 4. Analysis based on the energy balance equation is then performed, and a revised semiempirical model of the short-scale spectrum is developed and discussed in section 5. Conclusions are given in section 6.

2. Experiment

[7] The measurements were carried out during the autumn 2009–2012 in the Black Sea coastal zone using the Marine Hydrophysical Institute's research platform located 500 m offshore at 30 m depth.

[8] The spectra of short wind waves were derived from the stereophotographs of the sea surface applying the method proposed by *Kosnik and Dulov* [2011]. The stereo system consisted of two synchronized cameras SONY DSC-R1 with 72 mm focal length and angle of view $17° \times 11°$, rigidly fixed at 4.5 m height above the mean sea level. The camera spacing was 1.5 m, and the cameras observed the sea surface at $30°$ grazing angle. The overlapping area at the sea surface observed by both cameras was about 3 m $\times$ 4 m with the spatial resolution of 1–2 mm. The sea surface photography was accompanied with the measurements of wind velocity and frequency-directional wave elevation

spectra in the range from 0.05 to 1 Hz by an array consisting of six wire wave gauges.

[9] Table 1 summarizes the environmental conditions. The wind speed varied from 4 to 17 m/s. The orientation of the coastline is about $55°$, and winds blowing with directions between $69°$ and $200°$ and from $245°$ to $360°$ can be treated as onshore and offshore winds, respectively. The data presented here are mostly related to the onshore wind conditions.

3. Method for Short Wave Spectrum Retrieval

[10] The method is based on combination of well-known methods of stereo pair processing and mono-image brightness processing. The idea of stereo processing consists in finding the corresponding points in the simultaneously obtained stereo pair. Then, absolute coordinates (x, y, z) of the object at the sea surface can be found using classic triangulation algorithm [see, e.g., *Benetazzo*, 2006]. A vast set of corresponding points (some tens of thousands) enables us to reconstruct the surface for each stereo pair. Wave number spectrum of surface elevations can then be estimated from a long sequence of stereo pairs [see, e.g., *Banner et al.*, 1989]. Stereo imaging reconstruction of the sea surface was recently well developed and applied for a large number of scientific and technical goals (*Holthuijsen* [1983], *Benetazzo et al.* [2012], *Kosnik and Dulov* [2011], *Bechle and Wu* [2011], and many others). However, in field conditions, the only suitable objects at the sea surface are the brightness variations induced by surface waves. Therefore, a recovery of the surface topography of waves at a given scale requires the detection of brightness variations due to smaller-scale waves. This fact is the principal constraint for the spatial resolution of the stereo-based method. In particular, the shortest waves cannot be recovered because there are no smaller objects on the sea surface. In this paper, the wave spectrum derived from the stereo images is utilized for absolute calibration of the brightness spectrum of the same images. The determined transfer function (TF) is then used to retrieve the 2-D spectrum of the shorter waves that cannot be resolved by the single stereophotography technique (see *Kosnik and Dulov* [2011] for details and step-by-step algorithm).

[11] The approach is based on evaluating a linear relationship between the sea surface slopes, (ζ_x, ζ_y), and the sea surface brightness variations, I: $I = G_x\zeta_x + G_y\zeta_y$, where (G_x, G_y) are components of the mean surface brightness gradient [*Stilwell*, 1969; *Monaldo and Kasevich*, 1981]. In the Fourier space, this relation reads:

$$\tilde{I}(\mathbf{k}) = T(\varphi)k\tilde{\zeta}(\mathbf{k}), \tag{1}$$

where $T(\varphi)$ is a transfer function,

$$T(\varphi) = iG\cos(\varphi - \varphi_G), \tag{2}$$

[12] G is magnitude of the mean brightness gradient, φ_G is its direction, $\tilde{\zeta}(\mathbf{k})$ is amplitude of the Fourier harmonic of the sea surface displacement, and k and φ are modulus and direction of the wave number vector, $\mathbf{k}$. *Kosnik and Dulov* [2011] found a high correlation between stereo-derived surface elevation and the surface brightness

Table 1. Experimental Conditions[a]

Run Number	Date	Time	Wind Speed (m/s)	Wind Direction (North) (°)	Wind Direction (Stereo Base) (°)
1	6 Oct 2009	16:10–16:35	5.0	315	60
2	7 Oct 2009	10:15–10:40	9.9	70	80
3	13 Oct 2009	10:05–10:45	8.1	90	75
4	19 Oct 2009	16:00–16:20	14.4	70	80
5	26 Oct 2009	13:10–13:20	13.2	70	75
6	28 Oct 2009	14:50–15:10	7.1	345	65
7	4 Sep 2010	13:25–13:45	8.6	95	15
8	6 Sep 2010	13:50–14:05	5.0	200	150
9	10 Sep 2010	10:45–11:05	13	95	40
10	11 Sep 2010	11:05–11:25	15	100	30
11	12 Sep 2010	14:55–15:15	4	110	60
12	20 Sep 2010	09:45–10:05	10.0	101	20
13	24 Sep 2010	10:25–10:45	10.0	80	50
14	25 Sep 2010	11:30–11:55	9.0	95	55
15	19 Sep 2011	10:55–11:20	15.6	70	80
16	19 Sep 2011	12:55–13:10	17.2	70	80
17	20 Sep 2011	13:10–13:30	14.2	80	60
18	20 Sep 2011	15:15–15:35	12.0	80	125
19	21 Sep 2011	11:45–12:10	11.6	80	45
20	21 Sep 2011	13:40–13:55	11.0	80	45
21	22 Sep 2011	12:05–12:30	12.3	80	95
22	22 Sep 2011	14:15–14:35	13.9	80	95
23	25 Sep 2011	09:40–10:00	8.5	0	120
24	27 Sep 2011	11:00–11:20	11.5	90	80
25	27 Sep 2011	12:45–13:10	8.9	85	85
26	27 Sep 2011	15:10–15:25	7.6	85	85
27	7 Oct 2011	11:30–12:10	6.5	80	70
28	9 Oct 2011	11:30–11:50	12.8	75	85
29	11 Sep 2012	10:25–10:40	12.5	80	140
30	11 Sep 2012	12:35–12:55	11.1	85	140
31	11 Sep 2012	15:55–16:15	12.9	85	180
32	12 Sep 2012	10:50–11:10	14.2	90	130
33	12 Sep 2012	14:10–14:30	11.1	85	130
34	12 Sep 2012	16:40–17:00	10.7	90	180
35	17 Sep 2012	12:40–13:00	7.4	90	155
36	17 Sep 2012	15:20–15:40	8.0	90	190
37	18 Sep 2012	11:15–11:35	10.9	90	150
38	18 Sep 2012	13:00–13:15	6.5	90	180

[a]Data set 2009–2012.

variations in the range of wave numbers from 10 to 50 rad/m. Accepting that the brightness is linearly related to the surface slope, it is naturally to expand the transfer function (2) to higher wave numbers, because the nature of light refraction at smaller structures (capillaries, microwave breakings) remains the same as at decimeter and longer waves.

[13] Yet, the approach (1)–(2) works only in uniform sky conditions [*Stilwell*, 1969]. In our experiment, all the runs refer to clear sky situations or, less often, to 100% cloudiness. The Sun glint in the area of observation obviously could lead to violation of the accepted relations, and we also avoided this rotating the stereo system base. Nevertheless, in strong storm conditions few glitters still appeared in the view area due to enhanced local surface curvature. Such images, as well as the images with whitecaps and foam coverage, were excluded from consideration if the "spoiled" area reached some specified limit of about 2% of the total area. In other cases, the brightness spikes related to these features were replaced by lower brightness values.

Note, that though this procedure rarely led to significant data modifications, it might cause some spectrum underestimation at the highest winds because it filtered out the steepest breaking waves.

[14] If $S_{ZZ}(\mathbf{k})$ is a stereo-derived elevation spectrum and $S_{IZ}^{j}(\mathbf{k})$ are cross brightness-elevation spectra measured by left ($j = 1$) and right ($j = 2$) image of stereo pair, then from (1):

$$S_{IZ}^{j}(\mathbf{k}) = T_j(\varphi)kS_{ZZ}(\mathbf{k}). \qquad (3)$$

[15] This equation enables to estimate the transfer function for each camera, $T_j(\varphi)$, from stereo as

$$T_j(\varphi) = S_{IZ}^{j}(\mathbf{k})/[kS_{ZZ}(\mathbf{k})]. \qquad (4)$$

[16] The experimental estimates of the transfer function for left and right camera are shown in Figure 1. The model transfer functions defined by (2) are also shown in this figure. The model was fitted to the measurements by
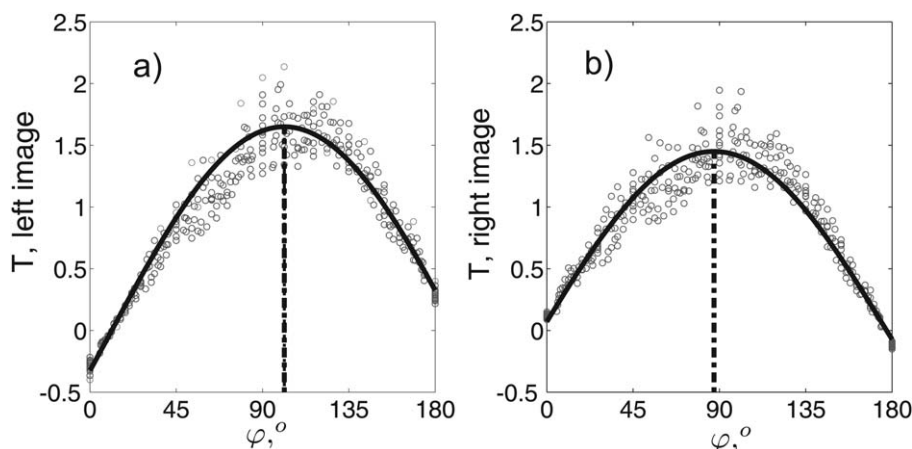
Figure 1. Experimental estimates of imaginary part of the transfer function (symbols) for (left) left and (right) right cameras calculated following equation (4) in the wave number range from 10 to 50 rad/m. Solid lines are model transfer function (2) fitted to the data. Vertical lines indicate the positions of maximum of transfer functions.

least-squares method (where G and φ_G are desired parameters). Notice a difference between the "phases" of the transfer function for the left and right cameras, which is about 15°.

[17] The relationship between the brightness spectra, $S_I^{i,j}(\mathbf{k})$, and the wave elevation spectra follows from (1) and reads:

$$S_I^{i,j}(\mathbf{k}) = T_i(\varphi) T_j^*(\varphi) k^2 S(\mathbf{k}), \qquad (5)$$

where repeated indexes indicate the autospectra and non-repeated ones indicate the cross-spectra.

[18] If observations are well separated in the azimuthal direction, φ_G in (2) is sufficiently different for each of the cameras. The spectrum of the sea surface slope, $k^2 S(\mathbf{k})$, can then be found directly from (5) by summing up the brightness autospectra obtained by each of the cameras:

$$k^2 S(\mathbf{k}) = \sum_i S_I^{i,i}(\mathbf{k}) / \sum_i T_i T_i^*. \qquad (6)$$

[19] Such a relation was successfully applied to retrieve 2-D surface wave spectra from sun-glitter imagery by *Bol'-shakov et al.* [1990].

[20] The brightness autospectra obtained by the left and right cameras are shown in Figures 2a and 2b. Dash lines in this figure show directions perpendicular to the mean brightness gradient, and the red lines indicate the wind direction. As it follows from this figure, the wind direction is well deviated from the line where the transfer function is vanishing. Moreover, there is a distinct difference between the mean brightness gradients for each of the transfer function. Therefore, one may anticipate that the wave spectrum derived from (6) is reliable. On the other hand, careful inspection of Figures 2a and 2b reveals well-visible noise at high wave numbers of order $k \sim 1000$ rad/m. As found (not shown here), wave spectra in the capillary range reconstructed with use of (6) can be significantly affected by this noise. Also, higher noise level at directions close to $\varphi_G \pm \pi/2$ prevents reliable estimation of anisotropy param-

eter (discussing below). Focusing on capillary-gravity wave spectra and their angular shapes, we thus avoid application of (6).

[21] As opposed to autospectra, a cross-brightness-spectrum shown in Figure 2c is much "cleaner," i.e., the noise at large wave numbers is not visible and noise in the vicinity of $\varphi_G \pm \pi/2$ is suppressed. Further, we consider the brightness cross-spectra,

$$S_I^{1,2}(\mathbf{k}) = T_1(\varphi) T_2^*(\varphi) k^2 S(\mathbf{k}). \qquad (7)$$

[22] Calculations of the cross-spectra require that left and right images are "well" matched in the horizontal plane. In this study, it was achieved by means of use of 10,000–20,000 reference points available from the stereo analysis [*Kosnik and Dulov*, 2011]. Though the absolute errors in the sea surface stereo reconstruction is of order of 1 cm [*Mironov et al.*, 2012], the spatial matching of the left and the right images obtained in our measurements was about half of centimeter due to interpolation of the images between the reference points. Such a good spatial matching is confirmed by values of the phase spectrum which are around zero in the wave number range $k < 1000$ rad/m (not shown here). This fact as well as rather high level of coherency of left and right images in the same range (see Figure 2d) justify validity of retrieval of the short wave spectra from the brightness cross-spectra in wave number range $k < 1000$ rad/m.

[23] In order to avoid unstable estimates of the wave spectra at azimuths where the transfer function product, $T_1(\varphi) T_2^*(\varphi)$, tends to zero, we use (7) with an a priori angular spreading function. In terms of the saturation spectrum, $B = k^4 S$, the spectrum takes the form:

$$B(k, \varphi) = B_0(k)[1 + \Delta \cos{(2(\varphi - \varphi_0))}]/\pi, \qquad (8)$$

where $B_0 = \int_0^\pi B(k, \varphi) d\varphi$ is the omnidirectional spectrum, Δ is a parameter ($0 < \Delta < 1$) to express the azimuthal modulation, and φ_0 is the general wave direction. Representation (8) takes the first term of Fourier expansion of the
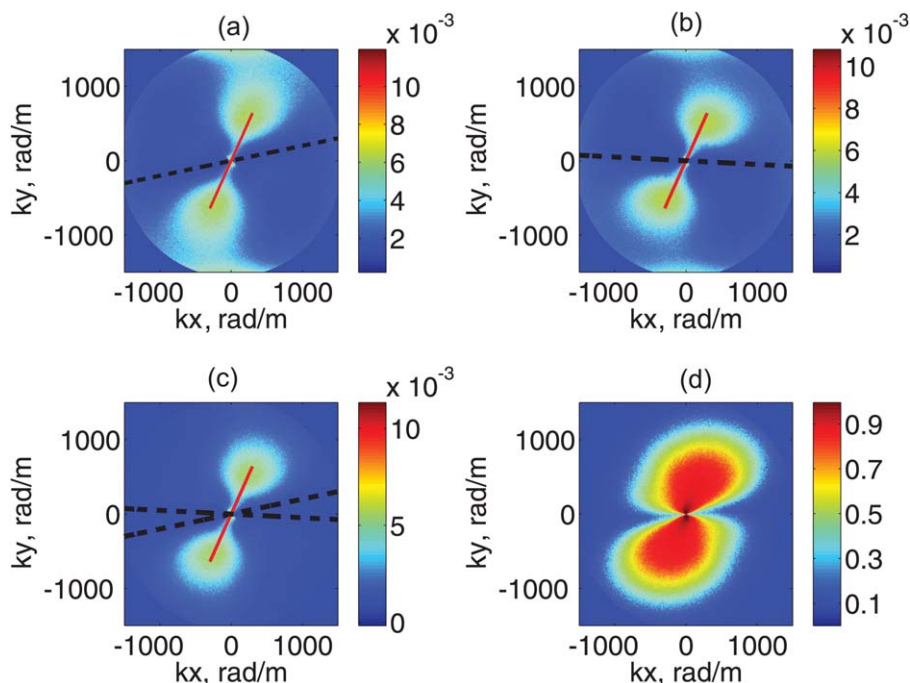
Figure 2. Run 6. Brightness spectrum of (a) left and (b) right images, (c) the real part of cross spectrum, and (d) square of coherence function between the brightness fields from left and right cameras. Dash lines indicate directions perpendicular to the direction of the mean brightness gradient. Red lines denote the wind direction.

folded spectrum, where odd harmonics vanish. The desired spectrum in a given wave number bin, $(k - dk, k + dk)$, is defined by three parameters: $B_0(k)$, φ_0, and Δ, which are found by fitting the observed cross-spectra using (7) and (8) with the known transfer functions, $T_1(\varphi)$ and $T_2^*(\varphi)$ (obtained from stereophotography measurements via relation (4)).

[24] Examples of this fitting procedure for two typical runs in three different wave number intervals are shown in Figure 3. In the case $\Delta = 0$, the angular shape of the transfer function product must coincide with the brightness cross-spectrum shape. Any deviation of $T_1(\varphi)T_2^*(\varphi)$ from the cross-spectrum indicates the directionality of the wave spectrum. As expected, the angular shape has a maximum close to the wind direction which may differ from the direction of the transfer function maximum. From (7), the angular shape of brightness cross-spectrum should have a maximum located between these two directions. To confirm this issue, two successive runs, 17 and 18, were made under the same wind direction and different view directions of the stereo rig. Except at the lowest wave numbers where the wave spectrum is less directional [*Banner et al.*, 1989; *Elfouhaily et al.*, 1997], this effect is well detected. Angular distributions of the brightness cross-spectra are shown in Figure 3.

4. Results

[25] Figure 4 illustrates examples of wave saturation spectra derived at two different wind speed conditions. Both spectra demonstrate well-pronounced directionality with spectral maximum aligned with the measured wind directions (see Table 1). A secondary capillary peak is well visible at lower wind speed (Figure 4a) and visually disappears at higher wind speed.

[26] Figure 5 shows omnidirectional spectra, main wave direction relatively to the wind direction, $\varphi_0(k) - \varphi_w$, and directionality coefficient, Δ, as a function of k, found after fitting the model cross-spectra (7) with (8) to the data as discussed above. Dash lines in this figure indicate 95% confidential intervals for the values estimated by the least square method. These intervals collapse at large k as the number of points used to solve equation (7) by the least squares method increases with increasing wave number. This is in contradiction with the increasing level of noise and decreasing value of coherence at higher wave numbers (see Figure 2d). We thus introduce an alternative measure of quality of the spectral estimates defined as the ratio between the standard deviation of the observed values of cross-spectra, $S_{IO}^{1,2}$, from its model fit, $S_I^{1,2}$, to the mean value, $\langle S_{IO}^{1,2} \rangle$:

$$R = \sqrt{\langle \left(S_{IO}^{1,2} - S_I^{1,2} \right)^2 \rangle} / S_{IO}^{1,2}, \qquad (9)$$

where the mean quantities are defined after averaging over the azimuth for a given k. Values of $R(k)$ are shown in Figure 5d. For all the runs, $R(k)$ is about 0.2, but it grows rapidly at $k \sim 1000$ rad/m. Therefore, we shall restrict the analysis to the wave number range $k < 1000$ rad/m.

[27] Omnidirectional spectrum (black solid line) in Figure 5a is derived from cross-brightness spectrum applying (7), while the gray squares indicate the stereo-derived spectrum in the range used for estimation of transfer function, $T(\varphi)$, with (4). As obtained for most cases, the local
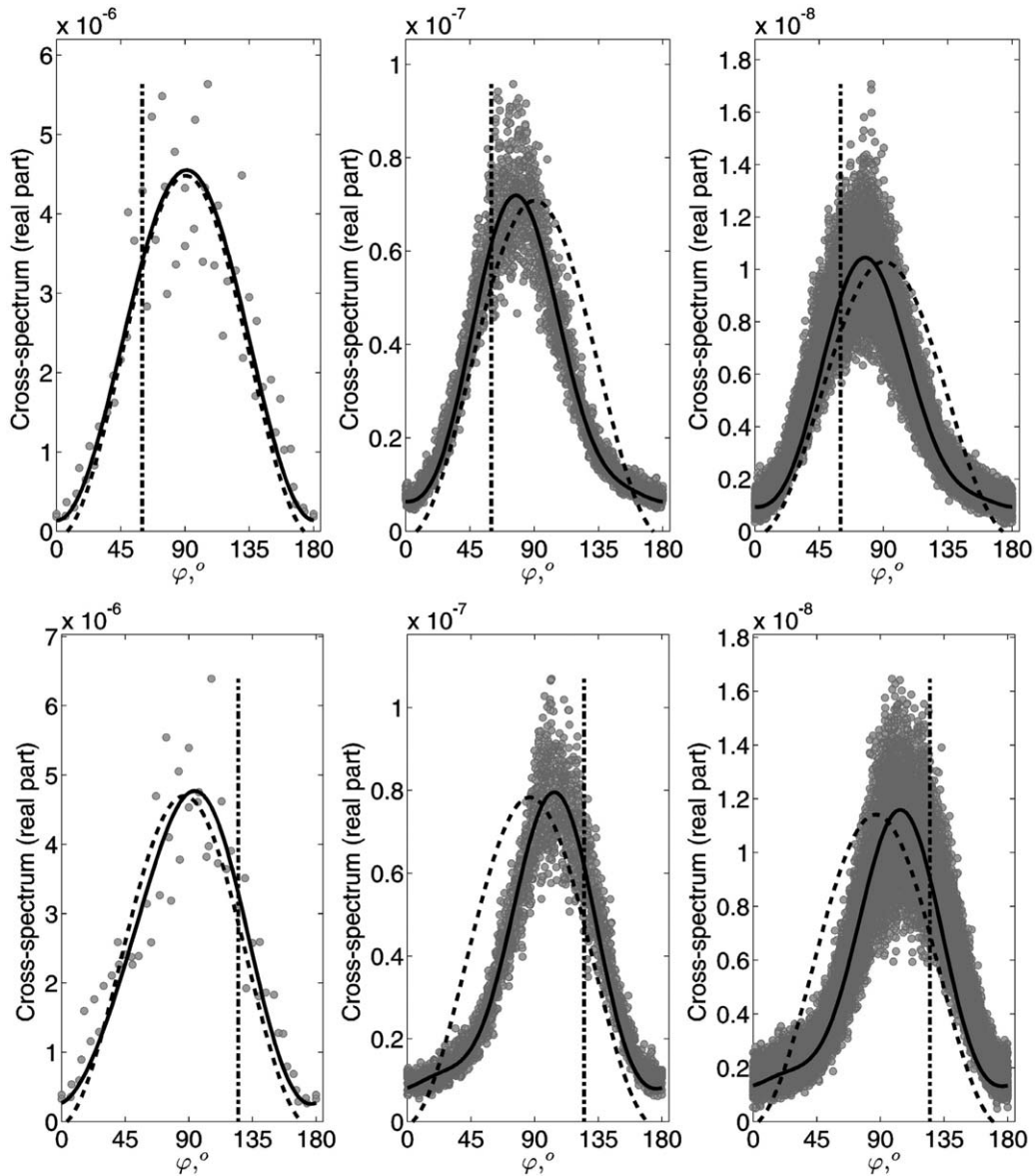
Figure 3. Brightness cross-spectra in the intervals (left) 25 rad/m $< k <$ 27 rad/m, (middle) 290 rad/m $< k <$ 310 rad/m, (right) 790 rad/m $< k <$ 830 rad/m for (top) run 17 and (bottom) run 18. Product of the transfer functions, $T_1(\varphi)T_2^*(\varphi)$, is shown by dash line. Model brightness cross-spectra defined by (7 and 8) and fitted to the data are shown by solid lines. Wind direction is indicated by vertical dash-dotted lines.

spectral peak direction, $\varphi_0(k)$, is aligned with the wind direction within the error of wind and stereo-base direction estimation (about 20°), except in the range $k < 100$ rad/m. For some cases, the energy of the folded spectrum in the cross-wind direction can exceed the energy in the along-wind direction. This manifests as a negative value of Δ, similar to what was found by *Banner et al.* [1989], and also consistent with *Hara et al.* [1998]. Shorter wave directionality gradually increases with larger k and, for this case, is maximum at $k \sim 800$ rad/m.

[28] Figure 6 (left) shows the spectral behavior of Δ-parameter averaged over all wind speeds. In general, our data demonstrate a monotonic trend of growth of the directionality with higher wave numbers. In the range of deci-

meter waves, the modulation coefficient is about zero or even negative, indicating that at cross-wind direction spectral level may be possibly larger than half of the along-wind direction spectral level. Such results are consistent with L-band (wavelength about 20 cm) radar measurements with cross-wind observations larger than down-wind ones [*Isogushi and Shimada*, 2009].

[29] To further compare this angular behavior of the observed wave spectra with azimuthal distribution of radar backscatter measurements, we hereafter propose to isolate the polarized contributions from radar signals. Indeed, polarization sensitivity is largely dominated by short wind waves. Practically, the total normalized radar cross section (NRCS), σ_0^{pp}, of the sea surface can be decomposed as
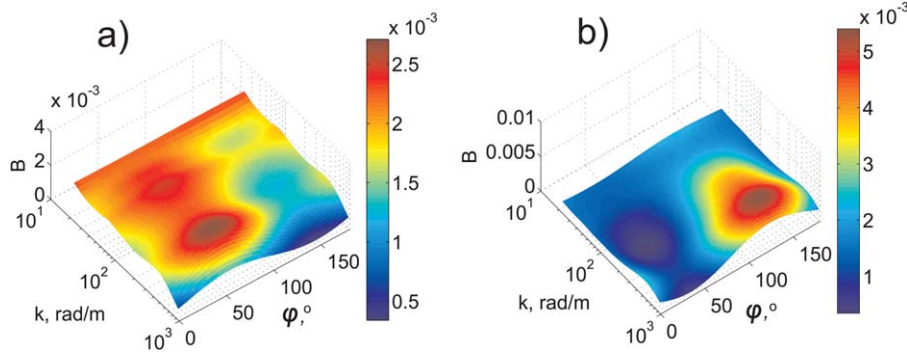
Figure 4. Directional curvature spectra in the coordinate system fixed to the stereo base. (a) Run 14, wind speed 9 m/s; (b) Run 18, wind speed 12 m/s.

$$\sigma_0^{pp} = \sigma_{br}^{pp} + \sigma_{wb}, \qquad (10)$$

where "pp" stands for horizontal transmit and receive (HH) polarization or vertical transmit and receive (VV)
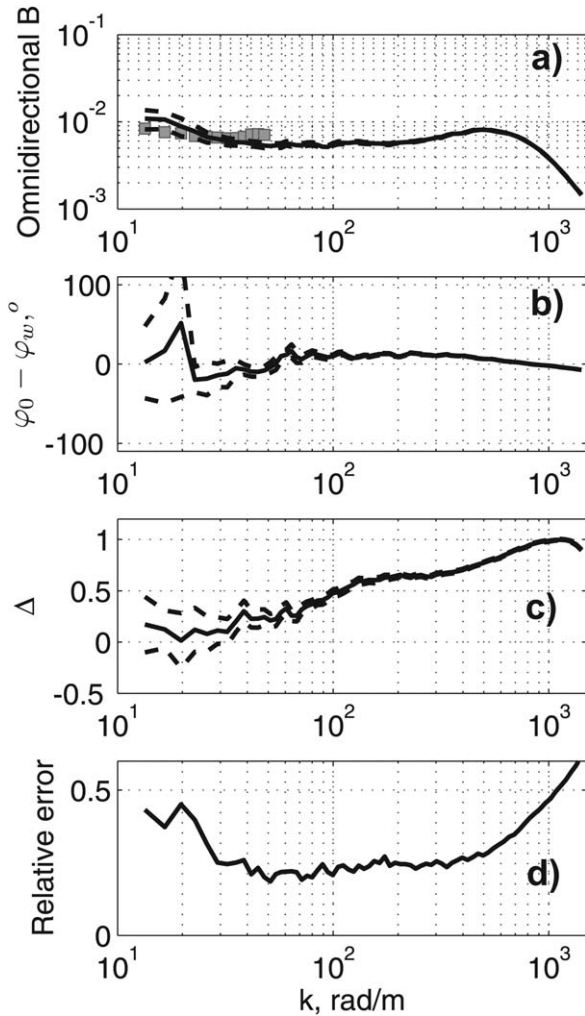
Figure 5. Run 12: (a) omnidirectional spectrum; (b) direction of the spectral maximum, $\varphi_0 - \varphi_{wind}$; (c) the anisotropy Δ-parameter; (d) the relative error defined by (9). Dashed lines show 95% confidential intervals. Gray squares in the upper plots indicate omnidirectional spectra derived from stereophotography.

polarization, σ_{br}^{pp} is the NRCS following the resonant Bragg scattering mechanism, and σ_{wb} is a nonpolarized contribution to the total NRCS. The polarized part operates as a filter of the wave saturation spectrum around the resonant wave number, k_{br}, linked to radar wave number, k_R, and incidence angle, θ, by the following relation: $k_{br} = 2k_R \sin \theta$. Thus, as suggested by, e.g., *Chapron et al.* [1997] and *Kudryavtsev et al.* [2013] and formally derived in *Guérin et al.* [2010] and *Bringer et al.* [2013], the polarization difference of the NRCS, $\Delta\sigma = \sigma_0^{vv} - \sigma_0^{hh}$, contains information about short wind wave saturation spectrum around Bragg wave numbers, i.e.,

$$\Delta\sigma = \sigma_{br}^{vv} - \sigma_{br}^{hh} = \left(G_{vv}^2 - G_{hh}^2\right)B(\mathbf{k}_{br}), \qquad (11)$$

where G_{pp}^2 are modified geometric scattering coefficient depending on incidence angle and modulation impacts (e.g., equation (31) in *Plant* [1986] or *Kudryavtsev et al.* [2003]). The extensive data set of copolarized (VV and HH) scatterometer data in Ku-band and C-band [*Quilfen et al.*, 1999; *Mouche et al.*, 2006] can then be used to compare azimuthal anisotropy and wind dependence of short wind waves spectrum around corresponding Bragg wavelengths. As obtained, Figure 6 (left), radar estimates are in very good agreement with the present optical measurements, but significantly different from some previous models (e.g., in *Elfouhaily et al.* [1997], see Figure 6, right plot).

[30] All retrieved omnidirectional saturation spectra are shown in Figure 7a. As found, the saturation spectra in the capillary-gravity range ($k > 100$ rad/m) are very sensitive to the wind speed, while in the decimeter wavelength range the spectral dependence on wind speed is much weaker. The present results apparently closely follow reported field measurements by *Hara et al.* [1998, Figure 8], especially for $k < 300$ rad/m (Figure 7b). However, comparison of our spectra in the capillary range with that were presented by *Hara et al.* [1998] reveals some remarkable difference. As mentioned in *Hara et al.* [1998], "it is rather surprising that at $u^* = 0.3$ m/s the degree of saturation increases rapidly (almost linearly) with k and reaches as high as 0.07 at $k = 800$ rad/m" and "it is of interest to see whether future wind wave measurements by other methods will yield similar high values in open ocean conditions." Our measurements do not show such high values in the capillary range as observed by *Hara et al.* [1998]. Furthermore, our data show explicitly a spectral roll-off at very large capillary wave number $k > 800$ rad/m. Similar spectrum behavior,
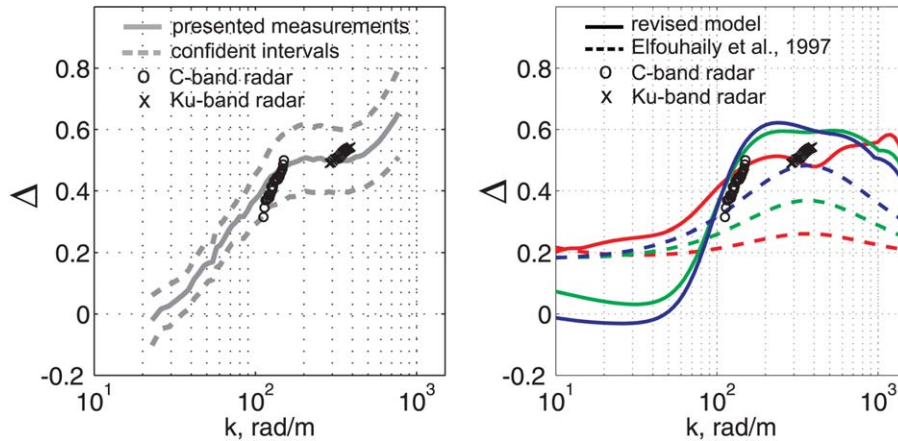
Figure 6. (left) Parameter of the angular anisotropy, Δ, derived from spectral measurements, (solid line with confident intervals shown by dash lines), and from C-band and Ku-band radar measurements (open circles and crosses correspondingly). (right) Parameter Δ following (dash lines) *Elfouhaily et al.* [1997] model and (solid lines) the revised model at wind speeds 5 m/s (red), 10 m/s (green), 15 m/s (blue). Symbols are the same as in the left plot.

but at lower wind speeds, was observed by *Hara et al.* [1998] (Figure 7b). Thus, we may anticipate that our observations provide a new valuable information about shape of the capillary wave spectra in the open ocean conditions.

[31] Comparisons with other semiempirical models of short wind wave spectra suggested by *Elfouhaily et al.* [1997], *Kudryavtsev et al.* [2003], and *Hwang* [2011] are shown in Figures 7c and 7d. In overall, the spectra are consistent, however, some remarkable differences in the angular spreading and spectral wind sensitivity between these models apparently exist.
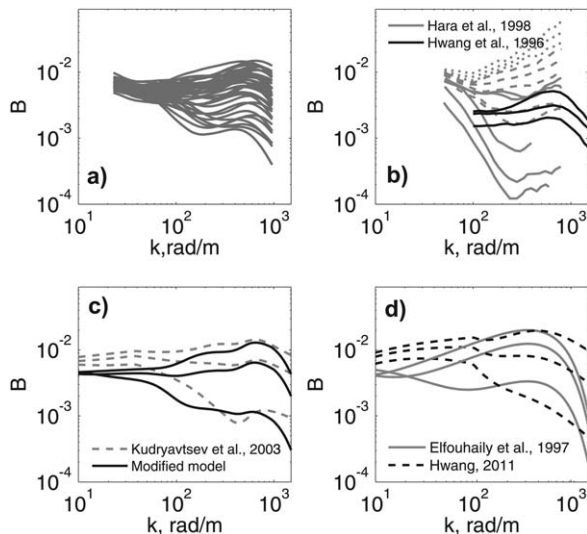

Figure 7. Omnidirectional wave number saturation spectra. (a) Present measurements; (b) field measurements by *Hwang et al.* [1996] (wind speeds are 2.1, 3.5, and 5.7 m/s) and by *Hara et al.* [1998], $u_* = 0.1, 0.2,$ and 0.3 m/s (notations are the same as in their Figure 8); (c) the revised model and model by *Kudryavtsev et al.* [2003] at wind speeds 5, 10, and 15 m/s; (d) model by *Elfouhaily et al.* [1997] and *Hwang* [2011].

[32] First, wind speed sensitivity has a clear spectral dependency and peaks in the capillary-gravity range. In this range, the wind sensitivity becomes significant and increases from low to moderate winds, to apparently level off at high winds. The spectral behavior of the wind exponent (the exponent m in $B \sim U_{10}^m$), averaged over all wind speeds and averaged over wind speeds below $U_{10} = 10$ m/s, are shown in Figure 8. Estimates derived from radar polarization difference for C-band and Ku-band data, as well as wind exponent obtained by *Banner et al.* [1989] are given. Analysis made by *Hwang* [2011], compiling different passive and active microwave measurements, is also shown to confirm an apparent consistency between wind exponents taken from these different sources.

[33] The integrated mean-square slopes of the sea surface, $MSS = \int B_0 k^{-1} dk$, calculated from the measured spectra in the wave number range from 20 to 1000 rad/m are shown in Figure 9. Using *Cox and Munk* [1954] data for the MSS of the clean (MSS_{CM}) and slick covered surface (MSS_{slick}), we simply estimate MSS in the short wind wave interval (MSS_{short}) as the difference: $MSS_{short} = MSS_{CM} - MSS_{slick}$. Though it is not exactly known what range of short wave is suppressed in the slick areas (shorter than about 30 cm, as discussed by the authors), we still may conclude that agreement of our measurements with *Cox and Munk* [1954] data is also good. Similar conclusion holds when considering Ka-band inferred MSS parameter of *Vandemark et al.* [2004]. Using Cox and Munk's directional MSS_{short} estimates, the integrated directionality, ratio of the MSS in cross-wind direction to the MSS in the upwind direction, is also in close agreement with the measured slope spectral directionality in wave number range $20 \ rad/m < k < 1000 \ rad/m$, as shown in Figure 9 (right).

[34] The total mean-square slope shown in Figure 9 (left) is calculated from the composition of the "long wave" spectra measured by the wave gauges and "short wave" spectra derived from the surface brightness measurements. The measured total MSS is in a good relation with the MSS reported by *Cox and Munk* [1954]. Measured MSS of the
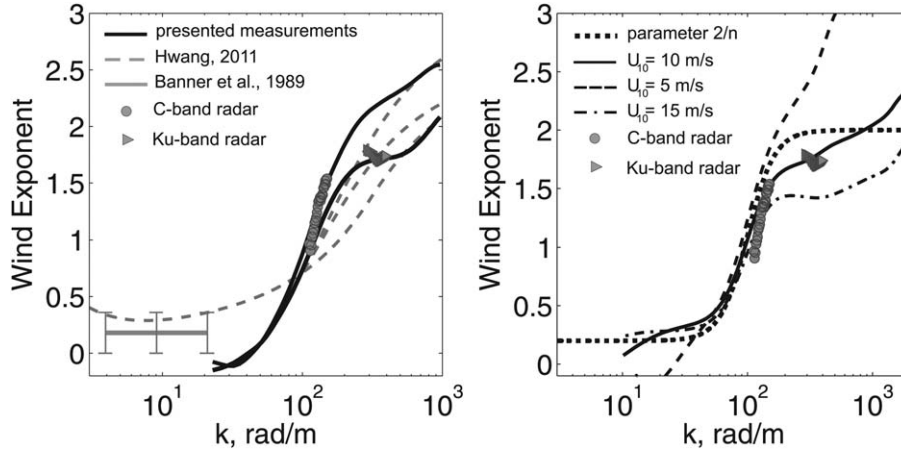
Figure 8. (left) Wind exponent in $B_0 \sim U_{10}^m$ for all runs (bottom solid line) and for winds lower 10 m/s (top solid line). Dash lines show wind exponent from *Hwang* [2011] model. Gray solid line with confidential intervals demonstrates *Banner et al*. [1989] result. (right) Revised model wind exponent. The model wind exponents correspond to $U_{10} = 5$ m/s (dash), $U_{10} = 10$ m/s (solid), and $U_{10} = 15$ m/s (dash-dotted). Dotted line in right plot shows parameter $2/n$. Symbols in both plots show wind exponent for Bragg scattering derived from C-band (circles) and Ku-band (triangles) data averaged around the wind speed 10 m/s.

sea surface confined the wave number intervals $k < 2000$ rad/m, $k < 162$ rad/m, $k < 63$ rad/m, $k < 21$ rad/m, are shown in Figure 10. Estimates of the MSS in the same intervals but derived from the radar measurements (as presented by *Hwang* [2011, Figure 4]) are also shown in Figure 10. In overall, our data are well consistent with radar observations.

[35] The mean surface curvature, $MC = \int B_0 k \, dk$, estimated in the wave number range $20 \; rad/m < k < 1000 \; rad/m$ is shown in Figure 11. These data are further used for validation of the model spectrum.

5. Revised Semiempirical Spectral Model

[36] These new measured spectra provide the opportunity to revise the previously suggested simplified semiem-

pirical models of short wind wave spectra suggested in *Kudryavtsev and Johannessen* [2004] and *Kudryavtsev et al*. [2005]. These model spectra follow on solutions of the energy balance under the wind action, generation of short waves by wave breaking, including generation of parasitic capillaries, viscous dissipation, nonlinear energy losses associated with wave breaking in the gravity range, and a nonlinear quadratic limitation of the spectral level in the capillary-gravity and capillary range. As developed, the resonant three-wave interaction term is omitted. Recently, *Kosnik et al*. [2010] investigated the role of this particular contribution. As found, efficiency of three-wave interactions is confined within a narrow band centered around the minimum phase velocity, causing, at low winds, a pronounced dip in the capillary-gravity saturation spectrum. At larger and smaller wave numbers resonant three-wave
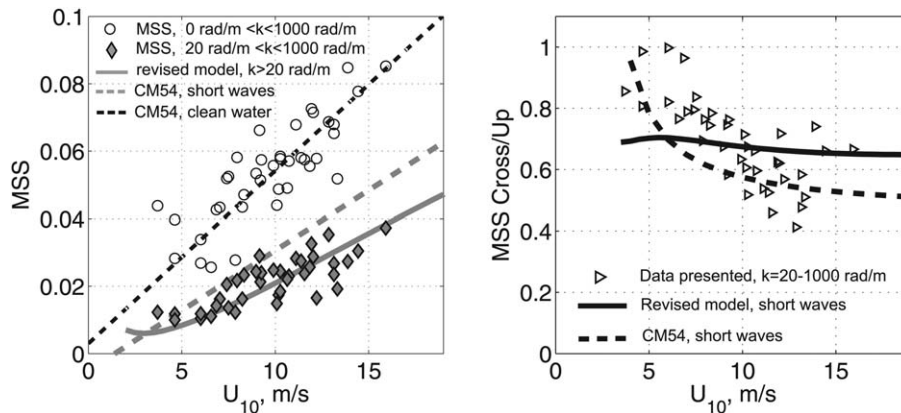
Figure 9. (a) Mean-square slopes of short waves (gray diamonds) and waves in the whole wave number region (circles). Dash black line is Cox and Munk relation [*Cox and Munk*, 1954], dash gray line is Cox and Munk relation for the short waves (see the text), solid line corresponds to model calculations. (b) Ratio of the MSS in cross-wind to the MSS in the up-wind direction for the short wind waves; dash lines—Cox and Munk data, symbols are the ratio estimated from measured spectra, solid line is the model.
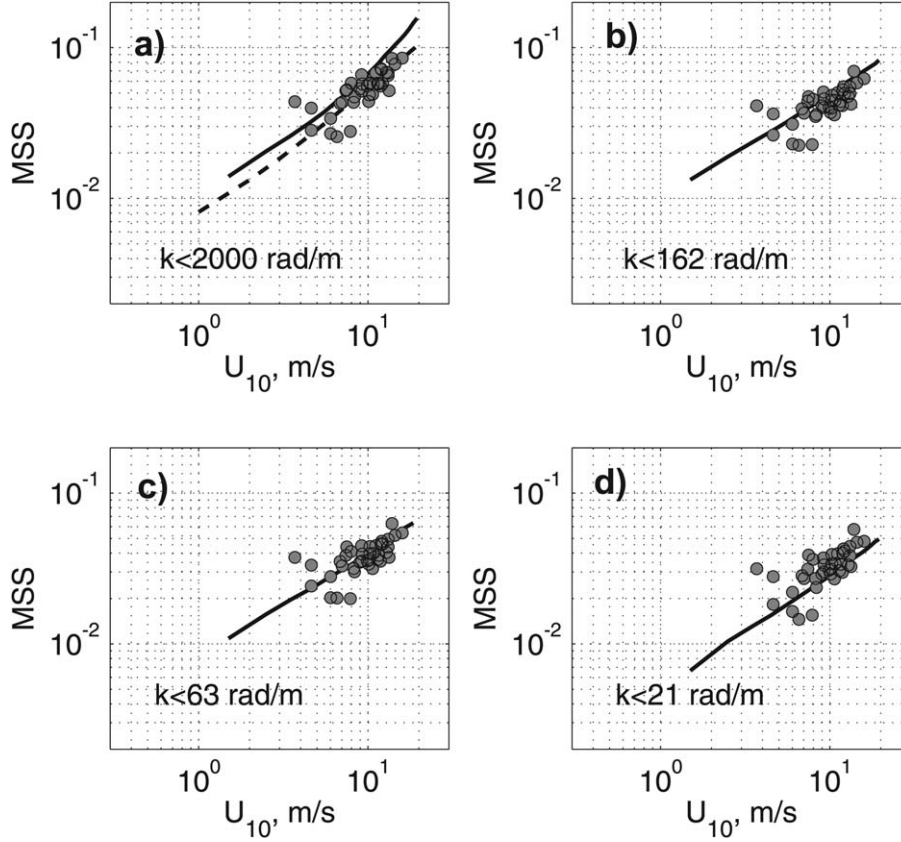
Figure 10. Mean-square slope of the sea surface confined various wave number intervals (indicated in each of the plots). Filled circles are present measurements; solid lines are fits to the data derived from the radar measurements (taken from *Hwang* [2011], his Figure 4); dash line is fit of *Cox and Munk* [1954] data.

interactions are weak compared to the combined impact of the other energy sources. In the present study, we thus omit this term to follow the same framework suggested earlier. As such, the wave spectrum is represented as a superposition of a spectrum corresponding to "freely propagating" waves generated by wind (direct wind forcing) and breaking of longer waves (due to mechanical disturbances of the surface) and a spectrum of "bound" parasitic capillaries generated by microscale breaking of the freely propagating waves (see Appendix A for more details and notations).

[37] The model has a "key" tuning function, $n(k/k_\gamma)$, corresponding to the exponent of the nonlinear dissipation term ($k_\gamma = \sqrt{g/\gamma}$ is the wave number of minimum phase velocity). This exponent then imposes the spectral dependency of the wind exponent, $B\tilde{u}_*^m$, in gravity and capillary-gravity range of the spectrum as $m = 2/n(k/k_\gamma)$ (see equation (A6) with (A2). Equation for $n(k/k_\gamma)$ is given by equation (A12) with (A13), and the fits to measured wind exponent in terms of $m = 2/n(k/k_\gamma)$ are shown in Figure 8. The other model tuning function, $\alpha(k/k_\gamma)$, sets up the "threshold level" for the saturation spectrum. As defined (see equation (A14)), this tuning function is not "free" as its shape is defined by $n(k/k_\gamma)$. The magnitude of $\alpha(k/k_\gamma)$ and consequently the wave spectral level further depends on the value of the tuning constant a. Value of this constant

is fixed at $a = 1.5 \cdot 10^{-3}$ to fit the model mean-square slope (MSS) to the measurements.

[38] Following the model construction, the wind exponent parameter, $m = 2/n(k/k_\gamma)$, also imposes the angular distribution, as $B(\cos \varphi)^{2/n}$ (see equation (A6)). The measured spectrum is a folded spectrum, $B_f(\mathbf{k})$, that relates to the directional spectrum as

$$B_f(\mathbf{k}) = [B(\mathbf{k}) + B(-\mathbf{k})]/2. \quad (12)$$

[39] The angular modulation parameter, Δ, of the folded spectra can be expressed through the directional spectrum in up-wind, down-wind, and cross-wind directions (spectra correspondingly) as

$$\Delta(k) = \frac{\pi}{2} \frac{B_{up} + B_d - 2B_{cr}}{B_o}, \quad (13)$$

where B_o is omnidirectional (integrated over all directions) spectrum. Anticipating that energy of waves traveling against the wind is comparably small (i.e., $B_{up} \ll B_d$), Δ is strongly dependent on spectral level in cross-wind directions. In these directions, the spectral level is assumed to be dominated by energy pumping from surface disturbances caused by breaking crests (see equation (A7)), as also suggested by *Rozenberg and Ritter* [2005] from laboratory experiments. Our experimental data (Figure 6) are used to infer the constant c_b in the energy source Q_b^w defined by
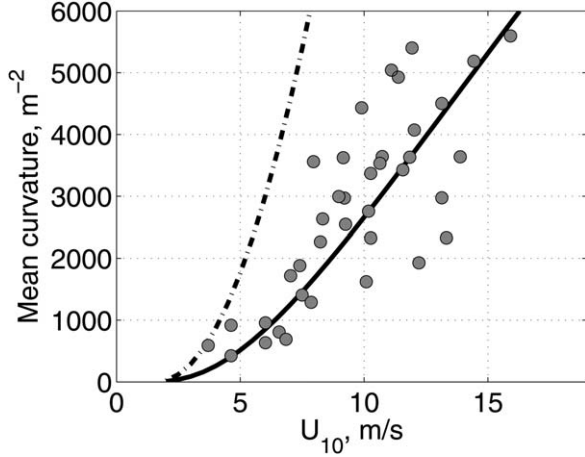
Figure 11. Mean curvature of the short waves: symbols are the data, solid and dash lines are the model mean curvature in the wave number range $20 \ \mathrm{rad/m} < k < 1000 \ \mathrm{rad/m}$ and $k > 20 \ \mathrm{rad/m}$, correspondingly.

(A5). This constant is fixed at $c_b = 4.5 \cdot 10^{-3}$ and determines an "overall" significance of wave breaking energy pumping mechanism. The spectral shape of Δ follows the nonlinear dissipation parameter $n(k/k_\gamma)$ tuned to the wind exponent data. Therefore, the azimuthal distribution of wave energy and its sensitivity to the wind are coupled.

[40] Model omnidirectional spectra are shown in Figure 7. As developed, model spectra well adjust to measurements to reproduce the spectral shape in the capillary-gravity and capillary interval. Figures 6 (right) and 8 (left) demonstrate the revised model consistency in terms of directionality parameter and wind exponent. Remarkably, the mean curvature of short wind waves calculated from the model spectrum in the wave number interval from $k = 20$ to $k = 1000$ rad/m corresponds to the mean curvature estimated from the measured spectra (Figure 11). Note that the total model mean curvature of the sea surface (integrated over all wave numbers) is about 2 times larger.

6. Conclusion

[41] In this paper, we report new field stereophotograph measurements of 2-D wave number spectra of short wind waves in the wavelength range from few millimeters to few decimeters. The method strongly builds on the brightness cross-spectral analysis to reduce the noise within this short wave gravity and capillary range. Field measurements of wind wave spectra are still rare, and the reported data thus provide valuable information to bring new evidences on the 2-D spectral distribution of short wind waves in the wavelength range from decimeters to millimeters.

[42] In particular, it is confirmed that spectra of decimeter waves are very weakly dependent on the wind speed and its direction. Wind speed and direction sensitivity only starts to appear in the short wavelength range, more precisely in the vicinity of the wave number 100 rad/m, where the wind exponent grows from 0.5 to 1.5–2.5 at 800 rad/m, and angular parameter amounts the value $\Delta \approx 0.5$. These aspects are very consistent with similar quantities derived from other optical and radar data. For the latter, we solely

extracted the polarization sensitivity to best isolate the contribution associated to the wave saturation spectrum around the resonant wave number. For the former, mean-squared slope statistics were used to assess the integrated short-scale directional spectral properties.

[43] As revealed, observed direction spectral distributions are significantly different from those previously suggested [*Elfouhaily et al.*, 1997; *Kudryavtsev et al.*, 2003, 2005]. On the basis of these new in situ measurements, we then propose to revise the semiempirical model of short wind wave spectra. Accordingly, new additional constraints are used to refine the nonlinear dissipation parameter, $n(k/k_\gamma)$, tuned to match the inferred wind exponent data. As hypothesized, such a constraint is key to refine the directional spectrum. The mean saturation spectrum is further adjusted to be consistent with the robust *Cox and Munk* [1954] dependence of mean-square slope on wind speed.

[44] As developed, the proposed two-dimensional wave number spectrum is valid over the ultragravity and capillary large wave numbers, and is analytically amenable to different usage. This revised model can readily be implemented in other studies (radar scattering, air-sea interaction issues, *etc*.), where detailed knowledge of short wind wave spectra is crucial.

Appendix A : The Main Relations of Semiempirical Spectrum Model

[45] Following the approach suggested by *Kudryavtsev and Johannessen* [2004] and *Kudryavtsev et al.* [2005], the spectrum results from solution of the energy balance equation written in the following form

$$Q(B) \equiv \beta_\nu(\mathbf{k})B(\mathbf{k}) - B(\mathbf{k})\left(\frac{B(\mathbf{k})}{\alpha}\right)^n + Q_b(\mathbf{k}) = 0, \qquad \text{(A1)}$$

where $Q(B)$ is the total spectral energy source represented as a sum of the effective wind forcing, nonlinear energy losses (associated with wave breaking in the gravity range, and a nonlinear quadratic limitation of the spectral level in the capillary-gravity and capillary range), generation of short waves by breaking of longer waves (Q_b), including generation of parasitic capillaries. In this equation $B(\mathbf{k})$ is the saturation spectrum, $\beta_\nu(\mathbf{k}) = \beta(\mathbf{k}) - 4\nu k^2/\omega$ is the effective growth rate, which is the difference between the wind growth rate, $\beta(\mathbf{k})$, and the rate of viscous dissipation, α and n are tuning functions of k/k_γ, which are equal to constants $\alpha = \alpha_g$, $n = n_g$ at $k/k_\gamma \ll 1$, and equal to other constants (e.g., $n = 1$) at $k/k_\gamma > 1$, $k_\gamma = \sqrt{g/\gamma}$ – wave number of minimum phase velocity.

[46] Wind wave growth rate is parameterized as suggested in *Kudryavtsev and Makin* [2004]:

$$\beta(\mathbf{k}) = c_\beta(1 + \cos^2\varphi)u_*(U_k\cos\varphi - c)/c^2, \qquad \text{(A2)}$$

where c_β is constant $(c_\beta = 1.2 \cdot 10^{-3})$, U_k is mean wind velocity at $z = k^{-1}$. The source term $Q_b = Q_b^{pc} + Q_b^w$ describes generation of short surface waves by wave breaking. Depending on the scale of a breaking wave, two mechanisms are specified. First, due to the effect of the surface

tension, short breaking waves with $k > k_b$ (where k_b is of order $k_b \sim 10^2$ rad/m) are not disrupted, but produce "regular" trains of parasitic capillaries (bound waves). These parasitic capillaries provide energy losses in breaking waves. Therefore, rate of generation of parasitic capillaries is equal to the energy dissipation by the carrying short gravity wave at wave number $K = k_\gamma^2/k$:

$$Q_b^{pc}(\mathbf{k}) = \phi(k)[B(B/\alpha)^n]_{k=K},\qquad (A3)$$

where $\phi(k)$ is a filter function restricting generation of parasitic capillaries in wave number space. The crests of longer breaking waves with wave number $k < k_b$ disrupt and produce mechanical perturbations of the sea surface. These mechanical perturbations generate "freely" propagating surface waves in all directions as reported by *Rozenberg and Ritter* [2005]. The rate of their generation is defined by

$$Q_b^\omega(\mathbf{k}) = c_b\omega^{-1}\int\int_{k<k_{bm}}\omega\beta(\mathbf{k})B(\mathbf{k})d\ln k\,d\varphi,\qquad (A4)$$

where c_b is an empirical constant (here $c_b = 4.5 \cdot 10^{-3}$); $k_{bm} = \min(k/10, k_b)$ is the upper limit of integration defining interval of breaking waves which generate freely propagating short waves at wave number k.

[47] We then assume that the wave spectrum in the equilibrium range, B, can be represented as a superposition of spectrum of freely propagating waves (generated by the wind per se and by wave breaking; hereinafter these waves are called as wind waves), B_w, and spectrum of parasitic capillaries (bound waves), B_{pc}, generated on the crests of that freely propagating waves:

$$B(\mathbf{k}) = B_w(\mathbf{k}) + B_{pc}(\mathbf{k}).\qquad (A5)$$

[48] Either $B_w(\mathbf{k})$ and $B_{pc}(\mathbf{k})$ spectra are defined as solution of the energy balance equation (A1). For the wind wave spectrum the wave breaking source Q_b in equation (A1) to be replaced by $Q_b = Q_b^w$. Solution of such a nonlinear algebraic equation is not straightforward (index of power has an arbitrary value). However, it can be effectively found by iterations on the basis of its known asymptotic solutions at up-wind, down-wind, and cross-wind directions. Aligned in the wind directions, the wave breaking source Q_b^w is expected to be small in comparison with direct wind energy input. Then approximate solution in down-wind direction is

$$B_w^d = \alpha\beta_\nu^{1/n}.\qquad (A6)$$

[49] At cross-wind directions, where the effective wind input is small or vanishing, $\beta_\nu \approx 0$, the wave spectrum approximately reads:

$$B_w^{cr} \approx \alpha^{n/(n+1)}(Q_b^w)^{1/(n+1)}.\qquad (A7)$$

[50] At the up-wind directions, where $\beta_\nu(\mathbf{k}) < 0$, one may anticipate the low spectral density, thus nonlinear term in equation (A1) can be omitted, and B_w results from the balance of wave breaking source and energy losses due to viscosity and interaction with the opposing wind:

$$B_w^{up} \approx -I_{wb}/\beta_\nu.\qquad (A8)$$

[51] Combination of these three "asymptotic" solutions,

$$B_w^0 = \max\left[B_w^d, \min\left(B_w^{cr}, B_w^{up}\right)\right],\qquad (A9)$$

provides a first guess for wave spectrum. Next iteration for wave spectrum is defined by

$$B_w^j = B_w^{j-1} - [Q(B_w)/(\partial Q/\partial B_w)]_{B_w=B_w^{j-1}},\qquad (A10)$$

where $Q(B_w)$ is the total energy source function (A1) for wind waves (where Q_b is equal to $Q_b = Q_b^w$). Practically, iteration scheme (A10) with the first-guess solution (A9) converges to the exact solution after three iterations.

[52] Spectrum of parasitic capillaries results from the same energy balance equation (A1) where the parasitic capillary term, $Q_b = Q_b^{pc}$, is the only energy source (wind forcing is omitted) which is balanced by viscous and nonlinear dissipation. Solution of this equation is straightforward and reads:

$$B_{pc}(\mathbf{k}) = \frac{\alpha}{2}\left[-4\nu k^2/\omega + \sqrt{(4\nu k^2/\omega)^2 + 4Q_b^{pc}(\mathbf{k})/\alpha}\right],\quad (A11)$$

with Q_b^{pc} defined by relation (A3) for the wind wave spectrum B_w.

[53] Now to complete the model we need to define the model functions, $n(k/k_\gamma)$ and $\alpha(k/k_\gamma)$, following *Kudryavtsev et al.* [2003]. The key function $n(k/k_\gamma)$ is related to the wind exponent (see equation (A6)): $m = 2/n(k/k_\gamma)$. We specify its shape as

$$1/n(k/k_\gamma) = (1 - 1/n_g)f(k/k_\gamma) + 1/n_g,\qquad (A12)$$

where $f(k/k_\gamma)$ is a tuning function satisfying conditions, $f \to 0$ at $k/k_\gamma \ll 1$, and $f \to 1$ at $k/k_\gamma \sim 1$. In order to fit wind exponent shown in Figure 8, the tuning function $f(k/k_\gamma)$ is defined as

$$f(k/k_\gamma) = [1 + \tanh(2(\zeta - \zeta_b))]/2,\qquad (A13)$$

where $\zeta = \ln k$, $\zeta_b = \ln k_b$ and k_b is a wave number corresponding to center of transition interval which is fixed at $k_b = 1/4k_\gamma$. Parameter n_g is fixed at $n_g = 10$ in order to be consistent with *Banner et al.* [1989] data.

[54] As argued in *Kudryavtsev et al.* [2003], the other tuning function, $\alpha(k/k_\gamma)$, is linked to $n(k/k_\gamma)$ as

$$\ln[\alpha(k/k_\gamma)] = \ln a - \ln(\overline{C_\beta})/n(k/k_\gamma),\qquad (A14)$$

with $\overline{C_\beta} = 0.03$ as a mean value of the growth rate, and a is a constant which is chosen as $a = 2 \cdot 10^{-3}$ in order to get right value of the sea surface MSS.

[55] The filter function $\phi(k)$ restricting action of the parasitic capillaries source (A3) is refined to be consistent with spectral behavior of f-function (A13) defining nonlinear dissipation. We assume that "high-frequency" cut-off of $\phi(k)$ must be linked to the transition wave number, k_b, as $k_{pc}^h = k_\gamma^2/k_b$, while the low-frequency cut-off of $\phi(k)$ to be $k_{pc}^l = nk_\gamma$ where n should be about $n = 2$, but we fixed it at
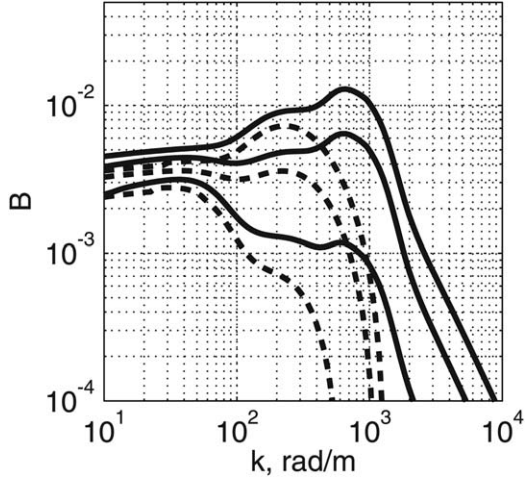
Figure 12. Model spectra for wind speeds $U_{10} = 5$ m/s, $U_{10} = 10$ m/s, $U_{10} = 15$ m/s (bottom-up). Calculation with and without wave breaking ripple generation term (solid lines and dash lines, respectively).

$n = 3/2$ in order to get location of the parasitic capillaries peak as observed in the experiment. Thus the filter function is defined as

$$\phi(k) = f\left(k/k_{pc}^l\right) - f\left(k/k_{pc}^h\right). \qquad (A15)$$

[56] An example of model spectra calculation is shown in Figure 12. The "pure wind" spectra are obtained when the impact of wave breaking on generation of the freely propagating waves and bound capillaries, is omitted. Compared with full model, the role of wave breaking is clearly emphasized.

[57] The suggested spectrum is valid in the equilibrium range of wind waves, i.e., far from the spectral peak of energy containing waves. In order to have the wave spectrum for the whole wave number range from wave of the spectral peak to shortest capillaries, B(**k**), we follow the approach suggested by *Elfouhaily et al*. [1997]: the full wave spectrum is a composition of the empirical spectrum, $B_p(\mathbf{k})$, proposed by *Donelan et al*. [1985] with the high-frequency "cut-off" function, $\varphi_p\left(k/k_p\right)$, suppressing B_p at wave numbers exceeding $10k_P$ (k_P is wave number of the spectral peak) and the equilibrium spectrum, B, suggested here. Then the model for the full wave spectrum is:

$$\mathrm{B}(\mathbf{k}) = \varphi_p B_p(\mathbf{k}) + \left(1 - \varphi_p\right)B(\mathbf{k}). \qquad (A16)$$

[58] Model calculations presented in section 4 are based on the composition (A16).

Appendix B : Error Analysis

[59] The procedure of image processing includes several stages and at each of them definite errors occur. The main error sources that appear in spectrum estimation with the use of proposed method are

[60] 1. The calibration error in stereo processing;

[61] 2. The parallax error, i.e., the inaccuracy in corresponding point search on the pair of images;

[62] 3. The error of brightness spectrum estimation due to foreign objects on the sea surface, glints, foam and brightness variation on the slope of longer waves;

[63] 4. Underestimation of brightness spectrum at higher wave numbers due to optical smoothing at several pixel scale;

[64] 5. The effects of nonlinearity of transfer function between image brightness and elevation.

[65] The first two points are analyzed in detail in *Mironov et al*. [2012] and give the error of order of 1 cm in horizontal direction and not more than several millimeters in wave height estimation. For our purposes, such accuracy is quite satisfactory because the pure stereo spectrum is used only in the range of few decimeter waves to obtain the transfer function between slope and surface brightness.

[66] From the other hand, the statistical error of elevation and image brightness omnidirectional spectra may be estimated as

$$\delta S_{stereo} = \sqrt{\frac{1}{N(N-1)}\sum_{i=1}^{N}\left(S_i - \overline{S}\right)^2}\Big/\overline{S}$$

and

$$\delta S_{br} = \sqrt{\frac{1}{N(N-1)}\sum_{i=1}^{N}\left(S_i - \overline{S_{br}}\right)^2}\Big/\overline{S_{br}},$$

[67] respectively, where N is the number of processed images in the run. Both these errors in most runs lie in the range 10–15%.

[68] As the transfer function, $T_{i,j}$, is calculated from the ratio of two spectra, its error estimate reads

$$\delta T = \sqrt{\delta S_{stereo}^2 + \delta S_{br}^2}$$

and does not exceed 20%. This value is obtained under the assumption of transfer function linearity that was shown and discussed in *Kosnik and Dulov* [2011]. Unfortunately, we cannot give the direct numerical estimation of the effects of transfer function nonlinearity but its $\cos^2$-shape, high-coherency level [*Kosnik and Dulov*, 2011] and adequate observed spectrum wind dependencies may serve to confirm that these effects are not crucial.

[69] One more error source manifests at the very shortest waves and related with camera imperfection. It consists in the fact that the point object in 3-D space is always seen on the photograph as a blurred spot of final size. In our case, it leads to spectrum underestimation at higher wave numbers [*Jähne*, 2002; *Kosnik and Dulov*, 2011]. In *Kosnik and Dulov* [2011], as well as in present paper, this problem was solved by spectrum multiplying by so called modulation (optical) transfer function (MTF) that was estimated in separate procedure. The error of its estimation may be calculated at every wave number the same way as above:

$$\delta_{MTF} = \sqrt{\frac{1}{N(N-1)}\sum_{i=1}^{N}\left(MTF_i - \overline{MTF}\right)^2}\Big/\overline{MTF}.$$

[70] Here, N is the number of photographs in MTF retrieval procedure, described in *Kosnik and Dulov* [2011].
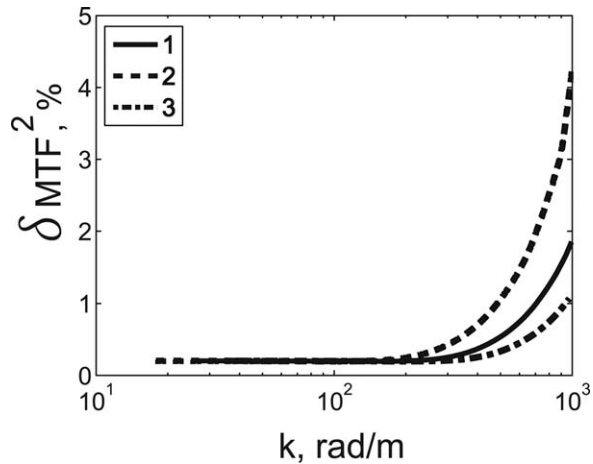
Figure 13. MTF error for the (1) middle, (2) top, and (3) bottom image parts.

δ_{MTF} was found to be negligibly low at wave numbers $k < 300$ rad/m (as well as the impact of MTF itself) and growing up to 5% at $k = 1000$ rad/m at the top area of the photo (Figure 13).

[71] Thus, the total error estimate for the omnidirectional saturation spectrum obtained from brightness spectrum is

$$\delta B = \sqrt{\delta T^2 + \left(\delta S_{br}^2 + \delta_{MTF}^2 \right)} \approx 30\%,$$

[72] slightly growing with the wave number in capillary range. The directional spectrum error is obviously higher and depends on the angle, increasing in the directions perpendicular to the main axis of stereo system [*Stilwell*, 1969; *Kosnik and Dulov*, 2011].

References

Banner, M. L., J. C. Trinder, and I. S. F. Jones (1989), Wave number spectra of short gravity waves, *J. Fluid Mech.*, *198*, 321–344, doi:10.1017/S0022112089000157.

Bechle, A., and C. Wu (2011), Virtual wave gauges based upon stereo imaging for measuring surface wave characteristics, *Coastal Eng.*, *58*(4), 305–316.

Benetazzo, A. (2006), Measurements of short water waves using stereo matched image sequences, *Coastal Eng.*, *53*, 1013–1032.

Benetazzo, A., F. Fedele, G. Gallego, P.-C. Shih, and A. Yezzi (2012), Offshore stereo measurements of gravity waves, *Coastal Eng.*, *64*, 127–138.

Bol'shakov, A., V. Burdjugov, S. Grodsky, and V. Kudryavtsev (1990), Two-dimensional surface elevation spectra from airphoto data, Izvestiya, *Atmos. Oceanic Phys.*, *26*, 652–658.

Breon, F. M., and N. Henriot (2006), Spaceborne observations of ocean glint reflectance and modeling of wave slope distributions, *J. Geophys. Res.*, *111*, C06005, doi:10.1029/2005JC003343.

Bringer, A., C.-A. Guerin, and A. Mouche (2012), Peakedness effects in near-nadir radar observations of the sea surface, *IEEE Trans. Geosci. Remote Sens.*, *50*(9), 3293–3301.

Bringer, A., B. Chapron, A. Mouche, and C.-A. Guerin (2013), Revisiting the short-wave spectrum of the sea surface in the light of the weighted curvature approximation, *IEEE Trans. Geosci. Remote Sens*, DOI 10.1109/TGRS.2013.2243459.

Chapron, B., V. Kerbaol, and D. Vandemark (1997), A note on relationships between sea-surface roughness and microwave polarimetric backscatter measurements: Results from polrad'96, in Proceedings of POLRAD International ESA Workshop, ESA WPP-135, Eur. Space Res. and Technol. Cent., Noordwijk, Netherlands, Apr 29.

Chapron, B., V. Kerbaol, D. Vandemark, and T. Elfouhaily (2000), Importance of peakedness in sea surface slope measurements and applications, *J. Geophys. Res.*, *105*, 17,195–17,202.

Cox, C., and W. Munk (1954), Measurement of the roughness of the sea surface from photographs of the sun's glitter, *J. Opt. Soc. Am.*, *44*(11), 838–850.

Donelan, M. A., and W. J. Pierson (1987), Radar scattering and equilibrium ranges in wind-generated waves with application to scatterometry, *J. Geophys. Res.*, *92*, 4971–5030, doi:10.1029/JC092iC05p04971.

Donelan, M. A., J. Hamilton, and W. Hui (1985), Directional spectra of wind-generated waves, *Philos. Trans. R. Soc. London A*, *315*, 509–562.

Elfouhaily, T., B. Chapron, K. Katsaros, and D. Vandemark (1997), A unified directional spectrum for long and short wind-driven waves, *J. Geophys. Res.*, *102*, 15,781–15,796, doi:10.1029/97JC00467.

Farrell, W. E., and W. Munk (2008), What do deep sea pressure fluctuations tell about short surface waves?, *Geophys. Res. Lett.*, *35*, L19605, doi:10.1029/2008GL035008.

Fung, A. K., and K. K. Lee (1982), A semi-empirical sea-spectrum model for scattering coefficient estimation, *J. Oceanic Eng.*, *7*(4), 166–176.

Guérin, C.-A., G. Soriano, and B. Chapron (2010), The weighted curvature approximation in scattering from sea surfaces, *Waves Complex Random Media*, *20*(3), 364–384.

Hara, T., E. J. Bock, and D. Lyzenda (1994), In situ measurements of capillary-gravity wave spectra using a scanning laser slope gauge and microwave radars, *J. Geophys. Res.*, *99*, 12,593–12,602, doi:10.1029/94JC00531.

Hara, T., E. J. Bock, J. B. Edson, and W. R. McGillis (1998), Observation of short wind waves in coastal waters, *J. Phys. Oceanogr.*, *28*, 1425–1438.

Holthuijsen, L. H. (1983), Observations of the directional distribution of ocean-wave energy in fetch-limited conditions, *J. Phys. Oceanogr.*, *13*, 191–207, doi:10.1175/1520-0485(1983)013¡0191:OOTDDO¿2.0.CO;2.

Hwang, P. (1993), Spatial measurements of short wind waves using a scanning slope sensor, *Dyn. Atmos. Oceans*, *20*, 1–23, doi:10.1016/0377-0265(93)90045-9.

Hwang, P. A. (2011), A note on the ocean surface roughness spectrum, *J. Atmos. Oceanic Technol.*, *28*, 436–443.

Hwang, P. A., S. Atakturk, A. Sletten, and D. B. Trizna (1996), A study of the wave number spectra of short water waves in the Ocean, *J. Phys. Oceanogr.*, *26*, 1266–1285, doi:10.1175/1520-0485(1996)026¡1266:ASOTWS¿2.0.CO;2.

Isogushi, O., and M. Shimada (2009), An L-band geophysical model function derived from PALSAR, *IEEE Trans. Geosci. Remote Sens.*, *47*(7), 1925–1936.

Jähne, B. (2002), Digital Image Processing, 5th Ed. Springer, NY.

Jähne, B., and K. S. Riemer (1990), Two-dimensional wave number spectra of small-scale water surface waves, *J. Geophys. Res.*, *95*, 11,531–11,546, doi:10.1029/JC095iC07p11531.

Kosnik, M. V., and V. A. Dulov (2011), Extraction of short wind wave spectra from stereo images of the sea surface, *Meas. Sci. Technol.*, *22*(1), 015504, doi:10.1088/0957-0233/22/1/015504.

Kosnik, M. V., V. A. Dulov, and V. N. Kudryavtsev (2010), Generation mechanisms for capillary–gravity wind wave spectrum, Izvestiya, *Fizika Atmos. Okeana*, *46*(3), 400–410.

Kudryavtsev, V., and J. Johannessen (2004), On effect of wave breaking on short wind waves, *Geophys. Res. Lett.*, *31*, L20310, doi:10.1029/2004GL020619.

Kudryavtsev, V., D. Hauser, G. Caudal, and B. Chapron (2003), A semiempirical model of the normalized radar cross-section of the sea surface: 1. Background model, *J. Geophys. Res.*, *108*, 8054, doi:10.1029/2001JC001003.

Kudryavtsev, V. N., and V. K. Makin (2004), Impact of swell on the marine atmospheric boundary layer, *J. Phys. Oceanogr.*, *34*, 934–949.

Kudryavtsev, V. N., V. K. Makin, and B. Chapron (1999), Coupled sea surface-atmosphere model: 2. Spectrum of short wind waves, *J. Geophys. Res.*, *104*, 7625–7640, doi:10.1029/1999JC900005.

Kudryavtsev, V. N., D. Akimov, J. Johannessen, and B. Chapron (2005), On radar imaging of current features: 1. Model and comparison with observations, *J. Geophys. Res.*, *110*, C07016, doi:10.1029/2004JC002505.

Kudryavtsev, V. N., B. Chapron, A. G. Myasoedov, and F. Collard (2013), On dual co-polarized SAR measurements of the ocean surface, *IEEE Geosci. Remote Sens. Lett.*, *10*(4), 761–765.

Lawner, R., and R. Moore (1984), Short gravity and capillary wave spectra from tower-based radar, *IEEE J. Oceanic Eng.*, *9*(5), 317–324.

Mironov, A. S., M. V. Yurovskaya, V. A. Dulov, D. Hauser, and C.-A. Guerin (2012), Statistical characterization of short wind waves from stereo images of the sea surface, *J. Geophys. Res.*, *117*, C00J35, doi:10.1029/2011JC007860.

Monaldo, F. M., and R. S. Kasevich (1981), Daylight imagery of ocean surface waves for wave spectra, *J. Phys. Oceanogr.*, *11*, 272–283, doi:10.1175/1520-0485(1981)0110272:DIOOSW2.0.CO2.

Mouche, A. A., D. Hauser, and V. Kudryavtsev (2006), Radar scattering of the ocean surface and sea-roughness properties: A combined analysis from dual-polarizations airborne radar observations and models in c band, *J. Geophys. Res.*, *111*, C09004, doi:10.1029/2005JC003166.

Mouche, A. A., B. Chapron, N. Reul, D. Hauser, and Y. Quilfen (2007), Importance of the sea surface curvature to interpret the normalized radar cross section, *J. Geophys. Res.*, *112*, C10002, doi:10.1029/2006JC004010.

Plant, W. J. (1986), A two-scale model of short wind-generated waves and scatterometry, *J. Geophys. Res.*, *91*, 10,735–10,749.

Quilfen, Y., B. Chapron, A. Bentamy, J. Gourrion, T. Elfouhaily, and D. Vandemark (1999), Global ERS 1 and 2 and NSCAT observations: Upwind/crosswind and upwind/downwind measurements, *J. Geophys. Res.*, *104*, 11,459–11,469.

Reul, N., and B. Chapron (2003), A model of sea-foam thickness distribution for passive microwave remote sensing applications, *J. Geophys. Res.*, *108*, 3321, doi:10.1029/2003JC001887.

Romeiser, R., W. Alpers, and V. Wismann (1997), An improved composite surface model for the radar backscattering cross section of the ocean surface: 1. Theory of the model and optimization/validation by scatterometer data, *J. Geophys. Res.*, *102*, 25,237–25,250, doi:10.1029/97JC00190.

Rozenberg, A., and M. Ritter (2005), Laboratory study of the fine structure of short surface waves due to breaking: Two-directional wave propagation, *J. Geophys. Res.*, *110*, C02011, doi:10.1029/2004JC002396.

Stilwell, D., Jr. (1969), Directional energy spectra of the sea from photographs, *J. Geophys. Res.*, *74*, 1974–1986, doi:10.1029/JB074i008p01974.

Trokhimovski, Y. G. (2000), Gravity capillary wave curvature spectrum and mean-square slope retrieved from microwave radiometric measurements (Coastal Ocean Probing Experiment), *J. Atmos. Oceanic Technol.*, *17*, 1259–1270, doi:10.1175/1520-0426(2000)0171259:GNCWCS2.0.CO2.

Trokhimovski, Y. G., and V. Irisov (2001), The analysis of wind exponents retrieved from microwave radar and radiometric measurements, *IEEE Trans. Geosci. Remote Sens.*, *38*(1), 470–479.

Vandemark, D., B. Chapron, J. Sun, G. H. Crescenti, and H. C. Graber (2004), Ocean wave slope observations using radar backscatter and laser altimeters, *J. Phys. Oceanogr.*, *34*, 2825–2842.

Voronovich, A. G., and V. Zavorotny (2001), Theoretical model for scattering of radar signals in Ku- and C-bands from a rough sea surface with breaking waves, *Waves Random Complex Media*, *11*(3), 247–269.

Zhang, X. (1995), Capillary-gravity and capillary waves generated in a wind wave tank: Observations and theories, *J. Fluid Mech.*, *289*, 51–82, doi:10.1017/S0022112095001236.